The Astronomical Journal, 129:2628–2635, 2005 June

DEEP SURFACE PHOTOMETRY OF M87 WITH 13 OPTICAL BANDS

Ying Liu,[1] Xu Zhou,[1] Jun Ma,[1] Hong Wu,[1] Yanbin Yang,[1] Jiuli Li,[1] and Jiansheng Chen[1]
Received 2004 November 1; accepted 2005 March 5

ABSTRACT

Multicolor surface photometry of M87 was undertaken with the Beijing-Arizona-Taiwan-Connecticut photometric system, which contains 13 optical bands covering a range from 3800 to 10000 Å. Radial profiles have been derived for surface brightness, ellipticity, position angle, and the residuals from the fitted ellipses. The results show a good agreement with pure elliptical isophotes for M87, and no obvious substructure or dust is detected out to $r = 500''$, corresponding to 40 kpc from the center. The surface brightness profile at $r < 190''$ is well fitted by the de Vaucouleurs law. Moreover, a cD envelope is detected outside that radius. Given the surface brightness profiles of the 13 bands, the spectral energy distribution (SED) of M87 is obtained as a function of semimajor axis (SMA). By fitting the observed SEDs to synthetic ones derived from the PEGASE model, we explored the star formation history (SFH) of this giant elliptical galaxy. In the hypothesis that the evolution time T of M87 is the same as the mean age of its globular clusters, about 14 Gyr, we find that the characteristic timescale τ of the SFH increases monotonically from 2 to 7 Gyr as a function of SMA, while the luminosity-weighted mean stellar ages range from about 11 to 9 Gyr in a mild decrease, and the mean stellar metallicity Z drops from 0.017 to 0.014 as the SMA increases to $r = 500''$. In the range $40'' < r < 190''$, the metallicity gradient $\Delta[\mathrm{Fe/H}]/\Delta[\log r] = -0.04$, while in the range $190'' < r < 400''$, the metallicity gradient $\Delta[\mathrm{Fe/H}]/\Delta[\log r] = -0.17$.

Key words: galaxies: evolution — galaxies: individual (M87) — galaxies: stellar content — galaxies: structure

1. INTRODUCTION

The investigation of the surface brightness distribution of early-type galaxies is of great importance in research on their intrinsic properties (Bender & Möllenhoff 1987). The color distributions in galaxies provide clues on their stellar population and chemical evolution. With the aid of linear detectors, CCDs, one can measure the surface brightness accurately and demonstrate the color gradient. The cause of color gradients is essentially the population gradients within galaxies. It has long been known that most galaxies become bluer as the galactocentric radius increases (Strom et al. 1976; Franx et al. 1989); early-type galaxies are typical cases for such an investigation of color gradient, with dust playing a negligible role.

M87 (NGC 4486) is a giant elliptical galaxy that is located in the center of the Virgo Cluster. It has been extensively probed at various wavelengths. The central region of M87 aroused considerable studies on its jet, black hole, nuclear disk, and temperature structures (Sparks et al. 1996; Meisenheimer et al. 1996; Perlman et al. 2001; Harms et al. 1994; Ford et al. 1994; Stewart et al. 1984; Belsole et al. 2001). Research on the rich globular clusters (GCs) in M87 was carried out to probe its mass distribution (Romanowsky & Kochanek 2001). Investigations of the populations of its GCs led to conclusions that they are of a coeval age of about 14 Gyr (Cohen et al. 1998; Jordán et al. 2002) and suggest different scenarios for their formation history (Forbes et al. 1997; Harris et al. 1998). However, the studies on the stellar populations of M87 have not kept pace with work that focuses on the central region and GCs to probe its formation scenario as a whole.

The surface brightness profile of M87 was reported to follow the $r^{1/4}$ law (de Vaucouleurs & Nieto 1978; Surma et al. 1990) with $r_e = 110''$ (Peletier et al. 1990a). Photographic plate observations of M87 show the existence of nonsymmetric diffuse light in the halo extending to 100 kpc (Weil et al. 1997) and a cD envelope in the outer region where the surface brightness profile deviates from the $r^{1/4}$ law (Carter & Dixon 1978; de Vaucouleurs & Nieto 1978).

Surma et al. (1990) also reported the cD envelope of M87 from photometric work, but the limited size of their CCD field, $10' \times 15'$, introduced significant systematic truncation errors at the outmost measured radii. The tendency to overestimate the sky background for this extremely large object is a severe problem in attempts to derive its precise surface brightness profile. Accuracy in sky determination guarantees the validity of colors, especially those derived at faint light levels.

Our work, based on the Beijing-Arizona-Taiwan-Connecticut (BATC) Multicolor Sky Survey (see § 2 or Fan et al. 1996; Zheng et al. 1999 for details), takes advantage of a field of view of about 1 deg^2, giving us the ability to study morphological properties of galaxies on extended scales and overcome the problem in sky background determination. Compared with previous work on M87, we attempted to measure the surface brightness profile, as well as its morphology characteristics at larger radii.

Previous studies on M87 produced the morphological parameters and revealed its color becoming gradually bluer outward from the center (Carter & Dixon 1978; Boroson et al. 1983; Davis et al. 1985; Peletier et al. 1990a, 1990b). The color gradient is about 0.15 mag in $B - R$ between the innermost region and $\log r = 1.7$ (Davis et al. 1985). However, the deduction of stellar populations from broadband colors is not straightforward, because contributions of various kinds of stars can hardly be disentangled within the wide bandwidth (Peletier et al. 1990a). This motivated our work with multicolor and large-field photometry on M87. Using the system of 13 optical bands makes it possible to obtain the spectral energy distributions (SEDs) of this giant galaxy. With the aid of the PEGASE model, we explored the star formation history (SFH) of M87 on an extended scale.

This paper is structured in five main parts. Details of observations and data reduction are presented in § 2. A literature comparison with previous work is done in § 3. The SFH of M87 is

[1] National Astronomical Observatories, Chinese Academy of Sciences, Beijing, 100012, China; liuying@vega.bac.pku.edu.cn.

TABLE 1

BRIEF OBSERVATION LOG OF M87 WITH CENTRAL WAVELENGTH λ_c AND THE rms ERROR OF THE FLUX CALIBRATION

No. (1)	Name (2)	λ_c (Å) (3)	Bandwidth (Å) (4)	Total Exposure (s) (5)	No. Images (6)	No. Nights (7)	rms (mag) (8)
1.....	*b*	3894	266	6000	5	1	0.02
2.....	*c*	4210	282	8400	7	1	0.02
3.....	*d*	4546	355	9600	8	1	0.01
4.....	*e*	4872	347	10200	9	1	0.01
5.....	*f*	5250	331	9600	8	1	0.01
6.....	*g*	5785	271	10800	9	1	0.01
7.....	*h*	6075	289	10800	9	1	0.01
8.....	*i*	6710	497	18000	15	2	0.01
9.....	*j*	7010	170	7200	6	1	0.02
10.....	*k*	7530	191	6000	5	1	0.01
11.....	*m*	8000	260	26400	22	3	...
12.....	*o*	9170	269	15600	13	1	0.01
13.....	*p*	9720	278	12600	11	1	0.02

discussed in § 4. The summary is presented in § 5. In this paper, we adopt a distance to M87 of 16 Mpc (Jacoby et al. 1992).

2. OBSERVATIONS AND DATA REDUCTION

2.1. *Observation and Image Reduction*

Large-field multicolor observations of the giant elliptical galaxy M87 were obtained with the BATC photometric system, which is based on a 60/90 cm f/3 Schmidt telescope located at Xinglong Station of the National Astronomical Observatories, Chinese Academy of Sciences (NAOC). This photometric system is characterized by its large field of view and multicolor systems. A Ford Aerospace 2048×2048 CCD camera is mounted at the focal plane. The field of view of the CCD is $58' \times 58'$ with a plate scale of $1''.7$ pixel^{-1}. The BATC filter system covers the optical bands from 3000 to 10000 Å (see Fan et al. 1996; Zhou et al. 2001). The filters are specially designed to avoid contamination from the brightest and the most variable night-sky emission lines. Images covering the whole optical body of M87 were accumulated in 13 optical bands, with a total exposure time of about 42 hr from 1996 February 23 to 2003 March 27. Most of the images are of exposure times 900–1200 s. A brief observation log is given in Table 1, which contains the filter name, central wavelength of the filter, total exposure time, etc.

To perform the flat-field correction, dome flat-field images were obtained by using a diffuse plate in front of the correcting

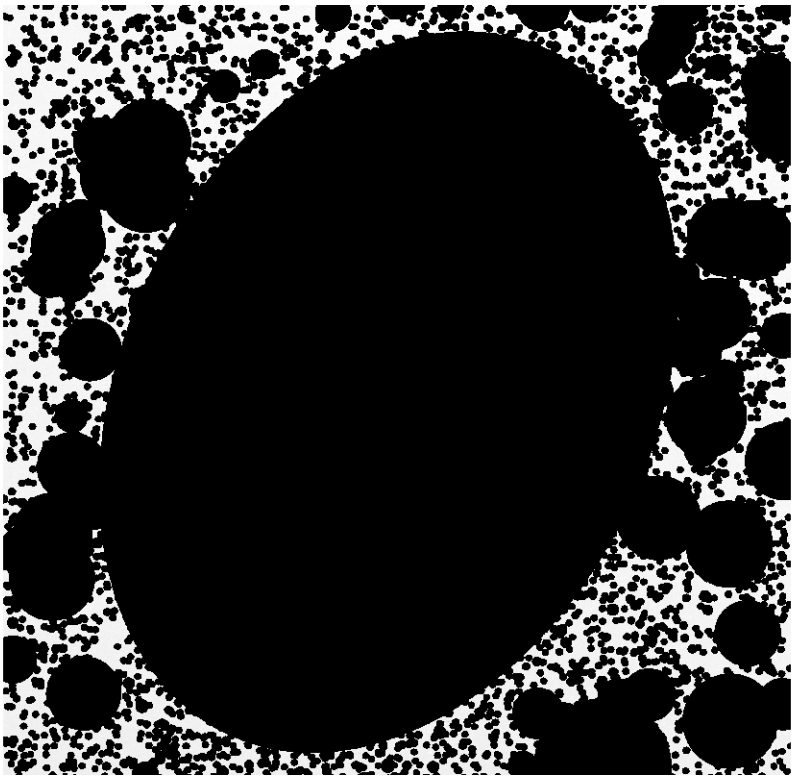

FIG. 1.—Full masked image of M87, blocking out all point sources as well as a large region around the galaxy itself.

TABLE 2
Error Estimation of Sky Background and the Radius where S/N = 6 in 13 Bands

Quantity	Band												
	b	*c*	*d*	*e*	*f*	*g*	*h*	*i*	*j*	*k*	*m*	*o*	*p*
$\sigma/\mathrm{flux}_{\mathrm{sky}}$ (%)	0.46	0.56	0.32	0.24	0.09	0.11	0.18	0.05	0.41	0.10	0.06	0.08	0.07
$\mathrm{flux}_{\mathrm{tr}}/\mathrm{flux}_{\mathrm{sky}}$ (%).....	0.6	1.3	0.7	1.7	1.8	1.0	1.0	1.6	1.0	0.14	0.3	1.0	0.3
$R_{\mathrm{S/N}=6}$ (arcsec).....	530	640	580	1550	1600	1200	1150	1600	1150	500	1000	1200	800

plate of the Schmidt telescope (Zhou et al. 2004). The raw images were first bias-subtracted and divided by the flat field. Then the images of the same band were combined. Most of the images of the same band were taken on one night. For those taken on different nights, the images were usually observed with a similar instrument system and observation conditions. There are only two bands for which data were taken on more than one night, and the accumulation of sky background does not show fluctuation of the sky pattern. The images of the same band were shifted to a common system during image combination, which accounts for dithered images and rotations in the CCD chip (Wu et al. 2002). The cosmic rays and bad pixels were corrected by comparison of multiple images in the process of image combination. All images were recentered and position-calibrated by using the field stars in the *Hubble Space Telescope* (*HST*) Guide Star Catalog (GSC; McLean et al. 1998).

For flux calibration, the Oke & Gunn (1983) standard stars were observed during photometric nights. The observations of these stars were used for flux calibration of the images taken at different bands (Zhou et al. 2001). The errors of calibration are listed in column (8) of Table 1. For the *m*-band image that lacks the observation of standard stars in this band, flux calibration was done by applying the method of model calibration that is specially developed for the large-field multicolor photometric system (Zhou et al. 1999).

2.2. *Sky Background Subtraction*

The sky background determination plays an important role in deriving accurate surface brightness, especially at faint light levels. To avoid any preconception in determining the surface brightness profile (Davis et al. 1985; Peletier et al. 1990a), a model-independent procedure was applied to get a two-dimensional sky background. The procedure consists of four main steps, similar to the method applied by Zheng et al. (1999) and Wu et al. (2002). The first involves star and galaxy masking. The IRAF package DAOPHOT was used to find all objects in our images with peak flux higher than 3 σ (the standard deviation of the local background). Background galaxies and saturated stars were identified by eye and masked with various apertures. M87 itself was masked using one ellipse. The final masked image is shown in Figure 1. The second step is the computation of median 50×50 pixel regions. A median filter of 50×50 pixels is convolved with the masked image using unmasked pixels to enlarge the fraction of area with sky background (Wu et al. 2002). In this way, some small masked regions are replaced by the surrounding background, and the available sky background increases. The third step is fitting the sky background with a first-order Legendre polynomial. After masking, we used the method of Zheng et al. (1999) to fit the sky background. Then we got a one-dimensional fitted image after the row-by-row fitting. The fourth step is smoothing the fitted image. To smooth the fluctuations introduced by the row-by-row polynomial fitting, the fitted image was convolved with a median filter of 1×100 pixels. This smoothed image was then adopted as the sky background and subtracted from the combined image.

To estimate the systematic error introduced by the sky background estimation, about 80 adjoining regions of 100×100 pixels were chosen to get the mean value ($\mathrm{flux}_{\mathrm{bg}}$) of the sky background–subtracted image. The standard deviation (σ) of $\mathrm{flux}_{\mathrm{bg}}$ of the 80 regions conveys information regarding how much the large-scale structure of the fitted sky background deviates from the true one. It is regarded as the systematic error introduced by sky background subtraction. Table 2 lists the ratio of the systematic error of sky subtraction, σ, to the mean sky level, $\mathrm{flux}_{\mathrm{sky}}$; the ratio of the mean flux, $\mathrm{flux}_{\mathrm{tr}}$, at the truncated radius $r = 500''$ to

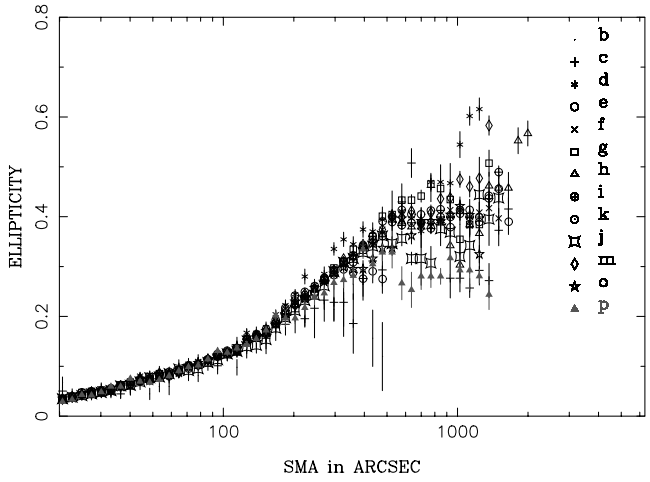

Fig. 2.—Ellipticity of M87 against SMA. Different symbols refer to the measurements in different bands.

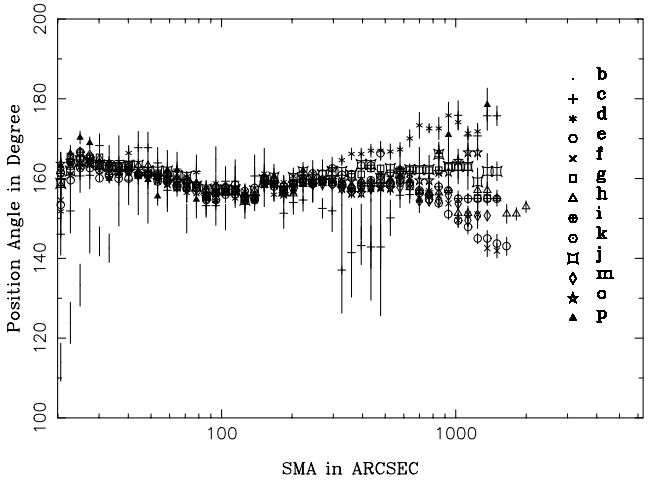

Fig. 3.—Position angle of M87 against SMA.

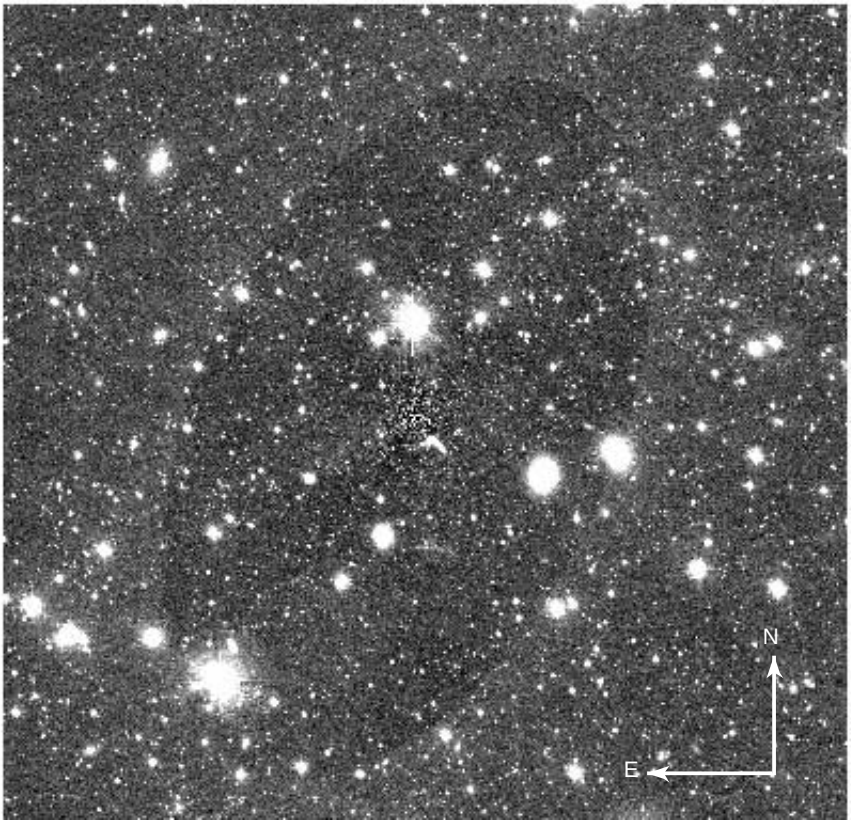

FIG. 4.—Residuals of the model-subtracted image of M87 in the *i* band. No substructure was found.

flux_{sky}; and the radius where the signal-to-noise ratio (S/N) = 6 in 13 bands.

2.3. *Photometry*

To unify the effects of seeing of different images, the FWHM values were normalized to the largest one, at radius 6″.2. After subtraction of sky background and removal of galaxies and foreground stars, the isophote analysis was carried out for each image in each band with STSDAS , a standard IRAF package. The isophote analysis yielded radial profiles of surface brightness, ellipticity, position angle, and the third- and fourth-order Fourier coefficients a_3, b_3, a_4, and b_4.

Figure 2 shows the ellipticity as a function of semimajor axis (SMA). M87 has a round central region but develops considerable ellipticities far from the center in our data, reaching 0.2 at a radius of about 200″ and 0.4 at 800″; by comparison, Cohen (1986) quotes a value of 0.21 at 192″.3, and Peletier et al. (1990a) gives 0.15 at 162″.3. The ellipticities in different bands agree well until 500″ from the center (40 kpc), implying that little dust exists in this region (Saraiva et al. 1999). The position angle keeps nearly constant at 160° with no more than 5° variation (see Fig. 3) at $r > 30''$. This agrees with the previous estimates carried out by other authors. King (1978) notes a value of 156° with a slight variation at radii beyond 30″. Davis et al. (1985) and Zeilinger et al. (1993) quote averaged position angles of 159° and about 160°, respectively.

The deviations from the isophotes of pure ellipses were analyzed for systematic components by means of Fourier transforms. The Fourier components reflect the asymmetry of the galaxy. The fourth-order cosine component b_4 is an indicator of the presence of subsystems, since $b_4 > 0$ indicates disky isophotes, and $b_4 < 0$ indicates boxy isophotes. In our work, a_3, b_3, a_4, and b_4 are zero at $r < 500''$ but show systematically larger scatters at larger radii.

The model image of M87, based on its surface brightness of the *i*-band profile, was subtracted from the image. No obvious substructure or debris was detected from the residuals in the model-subtracted image, as Figure 4 illustrates. The surface brightness profiles of other bands were derived by taking the *i*-band profile as a reference.

After the surface brightness profiles were derived, the colors of M87 in the BATC system were obtained by taking the flux ratio of all profiles with respect to the *i*-band profile, as shown in Figure 5. For clarity, only six bands (*d*, *e*, *i*, *g*, *m*, and *o*) were selected. The errors of the profiles were calculated by taking the

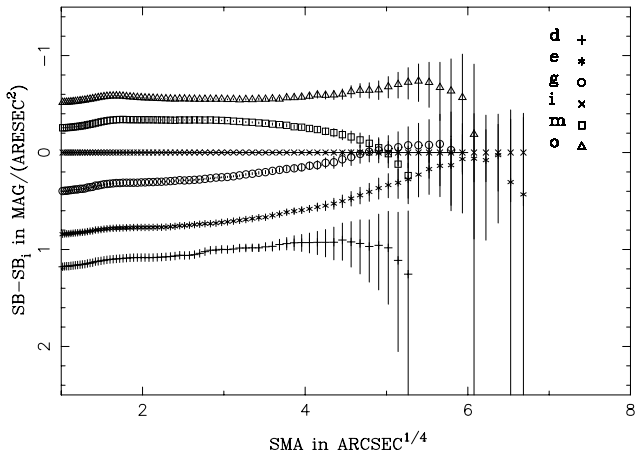

FIG. 5.—Colors of M87 in the BATC system as a function of SMA.

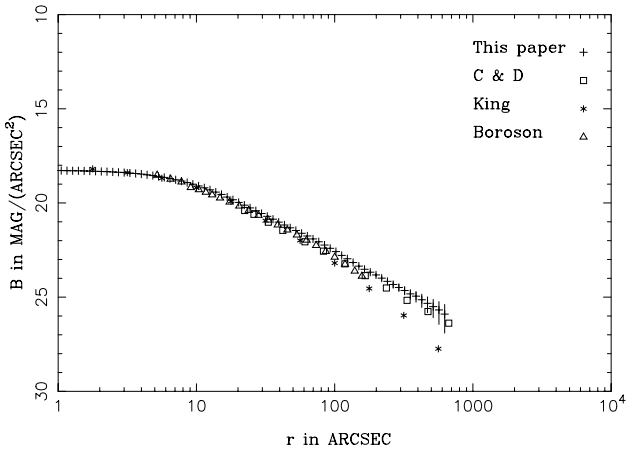

FIG. 6.—Surface brightness vs. radius in the *B* wave band, in which our observations are compared with those of several other observers. Surface brightnesses in magnitudes are plotted against log radius in arcseconds.

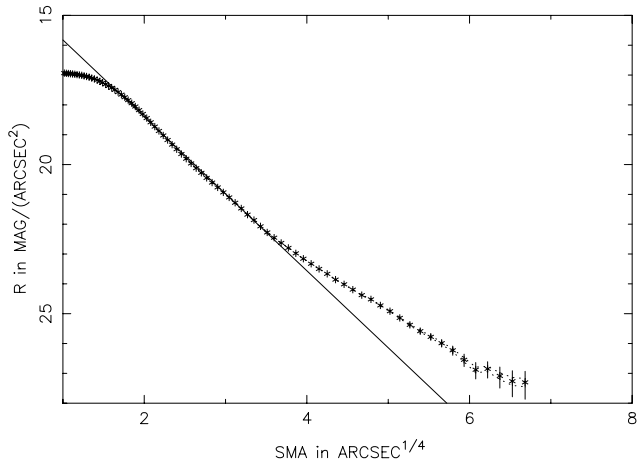

FIG. 8.—Surface brightness vs. radius in the *R* wave band. Asterisks represent the *R*-band profile, the solid line shows the best fitting of the $r^{1/4}$ law, and the dotted lines show the profiles with systematic errors taken into account.

sum of the errors contributed by sky background subtraction, calibration, and random errors.

3. COMPARISON WITH PREVIOUS WORK

For literature comparison, the surface brightness profiles were transformed to standard *UBVRI* bands using the transformation introduced by Zhou et al. (2003). The BATC *d*-band profile can be transformed to Landolt *B* band using $m_B = m_d + 0.2201(m_c - m_e) + 0.1278$ (Zhou et al. 2003). Figure 6 shows a comparison between our results and those of other observers, King (1978), Carter & Dixon (1978), and Boroson et al. (1983), in the *B* band. Our data agree well with the work of Carter & Dixon, but at large radii, we note discrepancies with the data of King, indicating that he may have subtracted slightly more sky background.

We also transformed the BATC *i*-band profile to Landolt *R* band using $m_R = m_i + 0.1048$ (Zhou et al. 2003). Figure 7 shows our data in the *R* wave band compared with the data of Boroson et al. (1983), Davis et al. (1985), and Peletier et al. (1990a). Apart from the agreement between our data and these most precise recent measurements, information on larger scales was obtained with our data. The color gradient in $B - R$ is 0.18 mag between the innermost region and $r = 100''$. Boroson et al. (1983) reported bluer color in $B - R$ by 0.15 mag between the innermost point and $\log r = 1.7$, and Peletier et al. (1990a) presents a bluer color in $(B - R)$ as 0.09 mag in the range $5'' < r < 150''$. The blue color presented by our system shows $(d - i) = 0.11$ mag in the range $40'' < r < 150''$.

We see a coronal component in M87 at $r > 190''$ (Fig. 8), inside which the profiles are well fitted by an $r^{1/4}$ law with $\mu_R = 13.23 + 2.58r^{1/4}$ (μ_R in magnitudes per square arcseconds and r in arcseconds). The smaller radius at which this envelope begins compared with other results can be explained by the relatively lower sky background subtracted by us. To illustrate the effect of systematic error introduced by sky background estimation, we give the profiles with this systematic error taken into account to estimate the validity of the detected cD envelope. In Figure 8 the asterisks represent the *R*-band profile, the solid line shows the best fitting of the $r^{1/4}$ law, and the dotted lines show the profiles with systematic errors taken into account. It is clear that the cD envelope is real and extends to about $r = 2000''$ (160 kpc). To perform the standard *V*-band luminosity, we transformed the BATC *g*-band profile to Landolt *V* band using $m_V = m_g + 0.3292(m_f - m_h) + 0.0476$ (Zhou et al. 2003). Assuming a constant mass-to-light ratio $M/L_V = 7.6$ if $A_V = 0.14$ (Binney & Mamon 1982), we calculated the integrated mass of the galaxy and the envelope. The mass profiles are given in units of

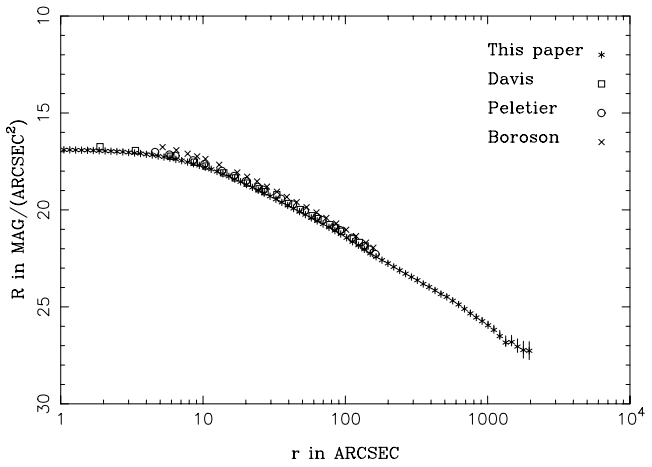

FIG. 7.—Surface brightness vs. radius in the *R* wave band, again comparing our results with those of other observers. The axes are as in Fig. 5.

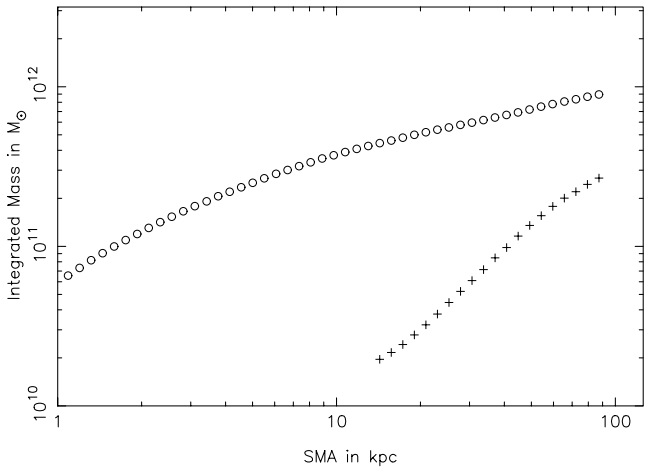

FIG. 9.—Integrated mass profiles of the galaxy (*open circles*) and the envelope (*crosses*) in solar masses.

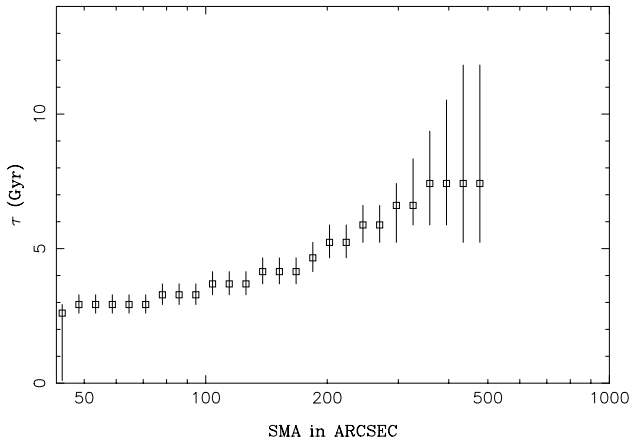

FIG. 10.—Quantity τ vs. SMA. The units of τ are gigayears and of SMA are arcseconds.

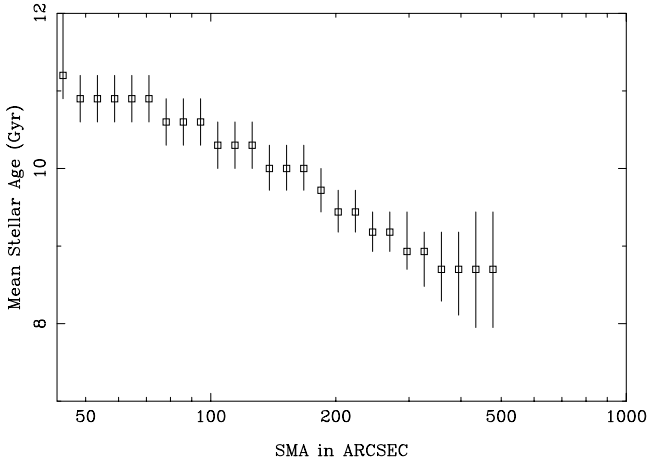

FIG. 11.—Mean stellar age in units of gigayears vs. SMA.

solar masses (see Fig. 9). Our result is mostly consistent with the gravitational mass (Matsushita et al. 2002).

4. STAR FORMATION HISTORY OF M87

With all the surface brightness profiles provided in different wave bands, we easily obtained the SEDs of M87 as a function of SMA. The SEDs of M87 were truncated at 500″ where the *k* band (7530 Å) S/N = 6, the least precise in the 13 wavebands.

The observed SEDs of M87 as a function of SMA make it possible to explore the stellar populations and the distribution of metallicity as a function of SMA. By fitting these observed SEDs with synthetic ones derived by using the PEGASE model (Fioc & Rocca-Volmerange 1997, 2000), we determined the SFH of this giant elliptical galaxy in an observational sense.

4.1. *Stellar Population Synthesis Model and Application*

PEGASE is an evolutionary spectral synthesis model for starbursts and evolved galaxies of the Hubble sequence. It covers an exceptionally large wavelength range from 220 up to 50000 Å. With the PEGASE code, we can derive the stellar SEDs of starbursts and evolved galaxies at any stage of evolution, within the initial metallicity range 0.0–0.1, with contributions of some factors like nebular emissions and galactic winds. Typical parameters of PEGASE are the star formation rate (SFR) and initial mass function (IMF). In this paper, we adopted Salpeter's IMF (1955), $\Phi(M) = AM^{-\alpha}$ with $\alpha = 2.35$, a lower cutoff $M_l = 0.1\ M_\odot$, and an upper cutoff $M_u = 125\ M_\odot$ (Sawicki & Yee 1998).

To simplify the scenario for the galaxy formation of M87, an evolutionary time $T = 14$ Gyr was kept fixed in the fitting of the model SEDs to each observed SED. Since this age was reported in work on M87's GCs (Cohen et al. 1998; Jordán et al. 2002) and was applied to investigation of the Virgo Cluster (Gavazzi et al. 2002), we assumed that the whole region of M87 has this common age. Correspondingly, the initial metallicity $Z_{\rm init}$ was set to zero. The SFH of M87 is explored by the parameter τ, which was set in a series of exponential grids (50 points, τ ranging from 0.01 to 30 Gyr). Other parameters were set to the defaults provided by PEGASE (Fioc & Rocca-Volmerange 1997; Li et al. 2004).

4.2. *Fitting Algorithm*

The synthetic spectra built from the models were convoluted with the BATC filter transmission curve to obtain the model flux in the BATC system. The model flux $L_i(\tau)$ in the *i*th BATC filter can be calculated with

$$L_i(\tau) = \frac{\int F_\lambda(\tau)\varphi_i(\lambda)\,d\lambda}{\int \varphi_i(\lambda)\,d\lambda}, \tag{1}$$

where $F_\lambda(\tau)$ is the flux derived from PEGASE at age $T = 14$ Gyr with SFR τ and $\varphi_i(\lambda)$ is the transmission curve of the *i*th filter in the BATC filter system.

The model SEDs in the BATC magnitude system were obtained and normalized for comparison with the observed galaxy SEDs. A foreground extinction of $E(B-V) = 0.022$ mag in the direction of M87 (Burstein & Heiles 1984) and the reddening law of Allen (1976, p. 264) were adopted in the extinction correction for observed SEDs.

To identify the parameters most likely representing the observed SEDs, a χ^2-minimization fitting was carried out by using

$$\chi^2 = \frac{1}{d}\sum_{i=2}^{15}\left[\frac{m_i^{\rm obs} - m_i^{\rm mod}(\tau)}{\sigma(i)}\right]^2, \tag{2}$$

where $m_i^{\rm mod}(\tau)$ is the relative magnitude in the BATC *i*th filter of a PEGASE model at age *T* with SFR τ, $m_i^{\rm obs}$ represents the observed magnitude of M87, $\sigma(i)$ is the *i*th uncertainty in the observed magnitude, and *d* is the number of degrees of freedom.

4.3. *Results*

Figure 10 plots the characteristic timescale τ as a function of SMA derived under the assumption that M87 possesses an evolution time $T = 14$ Gyr. The error bars were quoted at the 68% confidence level. The time over which the star formation takes place, τ, increases from about 2 Gyr in the center part to 7 Gyr at 40 kpc from the galactic center, which suggests that the duration of time over which star formation events take place increases as a function of SMA. In the center of the galaxy, the star formation finished in a shorter time than in the outer region of the galaxy. Gavazzi et al. (2002) explored the SFH for galaxies in the Virgo Cluster and reported $\tau = 3$ Gyr for elliptical galaxies. As evidenced by the luminosity-weighed mean stellar age plotted in our Figure 11, it is easy to tell that the longer the star formation events continue, the younger the mean stellar age is. The mean ages range from about 11 to about 9 Gyr in a mild decrease. Figure 12 illustrates the mean stellar metallicity *Z* as a function of SMA. The *Z* value drops steadily from about 0.017 to

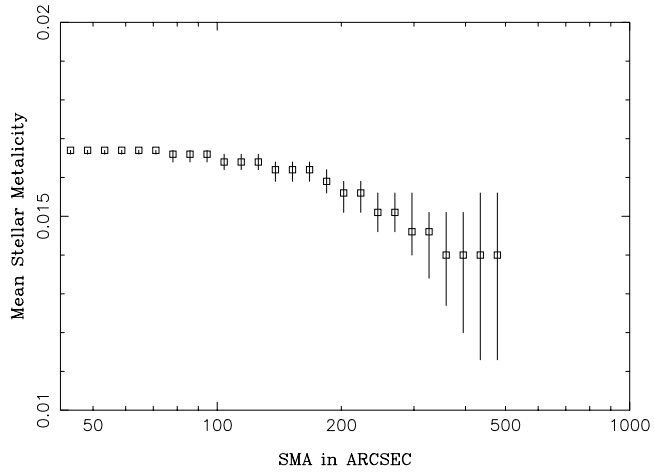

FIG. 12.—Mean stellar metallicity Z vs. SMA.

0.014 as SMA increases. From this figure, we also note that the metallicity gradient is composed by two components. In the range $40'' < r < 190''$, the metallicity gradient $\Delta[\mathrm{Fe/H}]/\Delta[\log r] = -0.04$, while in the range $190'' < r < 400''$, the metallicity gradient $\Delta[\mathrm{Fe/H}]/\Delta[\log r] = -0.17$. This metallicity scale was transformed from Z using the following formula (Carraro & Chiosi 1994):

$$\log Z = 1.03[\mathrm{Fe/H}] - 1.698. \quad (3)$$

Ignoring the values from the center to about $40''$ that were affected by the jet, which may not produce a reliable physical explanation, we can draw the conclusion from Figures 10–12 that the SFH of M87 is characterized by increasing timescale τ with mean stellar age and metallicity decreasing outward from the center. The slope of the metallicity gradient is consistent with the surface brightness profile, where a cD envelope begins at $r = 190''$.

Combined with the morphology and surface brightness profile of M87, the SFH derived under our assumptions suggests a continuous and steady formation history at least out to 40 kpc. In M87 star formation at large radii went on over a much longer time period than close in. The related findings concerning M87's GC system indicate similar evolutionary trends. Vesperini et al. (2003) found that for the M87 system, the ratio of blue to red GCs increases with radius. In addition, Côté et al. (2001) have found that the metal-poor GCs in M87 are more spatially extended than the metal-rich clusters. The two components seen in both the surface brightness profile and the metallicity gradient might suggest different formation scenarios for the galaxy and its envelope. Weil et al. (1997) also conclude that a different formation scenario is needed for the envelope of M87.

5. SUMMARY

In this paper, we perform large-field surface photometry of M87 with the BATC photometric system, which contains 13 optical bands covering a range from 3800 to 10000 Å. The results of photometry show M87 to be a typical giant elliptical galaxy embedded in an extended cD envelope. The morphology parameters suggest neither deviation from ellipse isophote nor substructure within $r = 500''$, corresponding to 40 kpc from its center. No diffused light or debris was detected in the model-subtracted image. The surface brightness profile is well fitted by the de Vaucouleurs law within $r = 190''$, and the cD envelope outside that radius is detected.

The colors of M87 become bluer outward from the center, as other authors witnessed. However, we track this trend to significantly greater than previous works. The observed SEDs of M87 were obtained as a function of SMA and truncated at 40 kpc from the center. Assuming a simple hypothesis, under which all regions of M87 have the same evolution time $T = 14$ Gyr and the initial metallicity $Z_{\mathrm{init}} = 0$ regardless of radius, we fit the model SEDs to each observed SED and get the SFH for M87. We find that the characteristic scale τ, which is an increasing function of SMA, ranges from 2 to 7 Gyr. The stellar mean age drops from 11 to 9 Gyr as SMA increases. The mean stellar metallicity decreases with SMA, a general phenomenon displayed by most elliptical galaxies. The Z value drops steadily from about 0.017 to 0.014 as SMA increases. The metallicity gradient is composed of two components: in the range $40'' < r < 190''$, the metallicity gradient $\Delta[\mathrm{Fe/H}]/\Delta[\log r] = -0.04$, and in the range $190'' < r < 400''$, the metallicity gradient $\Delta[\mathrm{Fe/H}]/\Delta[\log r] = -0.17$.

The results show a longer time period of star formation at large radii than close in and suggest a different formation scenario for the envelope of M87. However, the formation scenarios for this giant elliptical galaxy are still open to discussion until its stellar dynamics and other observational properties are taken into account for further investigation.

We highly appreciated Eric S. Perlman's insightful and helpful comments that greatly improved this manuscript. Albrecht Ruediger's help in English is acknowledged. We thank Yu Lu for valuable discussion.

This work has been supported by the Chinese National Key Basic Research Science Foundation (NKBRSF TG199075402) and in part by the Chinese National Science Foundation 10473012.

REFERENCES

Allen, C. W. 1976, in Astrophysical Quantities (London: Athlone Press)
Belsole, E., et al. 2001, A&A, 365, L188
Bender, R., & Möllenhoff, C. 1987, A&A, 177, 71
Binney, J., & Mamon, G. A. 1982, MNRAS, 200, 361
Boroson, T. A., Thompson, I. B., & Shectman, S. A. 1983, AJ, 88, 1707
Burstein, D., & Heiles, C. 1984, ApJS, 54, 33
Carraro, G., & Chiosi, C. 1994, A&A, 287, 761
Carter, D., & Dixon, K. L. 1978, AJ, 83, 574
Cohen, J. G. 1986, AJ, 92, 1039
Cohen, J. G., Blakeslee, J. P., & Ryzhov, A. 1998, ApJ, 496, 808
Côté, P., et al. 2001, ApJ, 559, 828
Davis, L. E., Cawson, M., Davies, R. L., & Illingworth, G. 1985, AJ, 90, 169
de Vaucouleurs, G., & Nieto, J. L. 1978, ApJ, 220, 449
Fan, X. H., et al. 1996, AJ, 112, 628
Fioc, M., & Rocca-Volmerange, B. 1997, A&A, 326, 950
———. 2000, preprint (astro-ph/9912179)
Forbes, D. A., Brodie, J. P., & Grillmair, G. J. 1997, AJ, 113, 1652
Ford, H. C., et al. 1994, ApJ, 435, L27
Franx, M., Illingworth, G., & Heckman, T. 1989, AJ, 98, 538
Gavazzi, G., Bonfani, C., & Sanvito, G. 2002, ApJ, 576, 135
Harms, R. J., et al. 1994, ApJ, 435, L35
Harris, W., Harris, G. L. H., & McLaughlin, D. E. 1998, AJ, 115, 1801
Jacoby, G. H., et al. 1992, PASP, 104, 599
Jordán, A., et al. 2002, ApJ, 576, L113
King, I. 1978, ApJ, 222, 1
Li, J. L., Ma, J., Zhou, X., Jiang, Z., Yang, Y., & Chen, J. 2004, A&A, 420, 89
Matsushita, K., Belsole, E., Finoguenov, A., & Böhringer, H. 2002, A&A, 386, 77
McLean, B., Hawkins, C., Spagna, A., Lattanzi, M., Lasker, B., Jenkner, H., & White, R. 1998, in IAU Symp. 179, New Horizons from Multi-Wavelength Sky Surveys, ed. B. J. McLean et al. (Dordrecht: Kluwer), 431
Meisenheimer, K., Roeser, H.-J., & Schloetelburg, M. 1996, A&A, 307, 61

Oke, J. B., & Gunn, J. E. 1983, ApJ, 266, 713
Peletier, R. F., Davies, R. L., Illingworth, G. D., Davis, L. E., & Cawson, M. 1990a, AJ, 100, 1091
Peletier, R. F., Valentijn, E. A., & Jameson, R. F. 1990b, A&A, 233, 62
Perlman, E. S., Biretta, J. A., Sparks, W. B., Macchetto, F. D., & Leahy, J. P. 2001, ApJ, 551, 206
Romanowsky, A. J., & Kochanek, C. S. 2001, ApJ, 553, 722
Salpeter, E. E. 1955, ApJ, 121, 161
Saraiva, M. F., Ferrari, F., & Pastoriza, M. G. 1999, A&A, 350, 399
Sawicki, M., & Yee, H. K. C. 1998, AJ, 115, 1329
Sparks, W. B., Biretta, J. A., & Macchetto, F. 1996, ApJ, 473, 254
Stewart, G. C., Fabian, A. C., Nulsen, P. E. J., & Canizares, C. R. 1984, ApJ, 278, 536
Strom, K. M., Strom, K. M., Goad, J. W., Vrba, F. J., & Rice, W. 1976, ApJ, 204, 684
Surma, P., Seifert, W., & Bender, R. 1990, A&A, 238, 67
Vesperini, E., Zepf, S. E., Kundu, A., & Ashman, K. M. 2003, ApJ, 593, 760
Weil, M. L., Bland-Hawthorn, J., & Malin, D. F. 1997, ApJ, 490, 664
Wu, H., et al. 2002, AJ, 123, 1364
Zeilinger, W. W., Moller, P., & Stiavelli, M. 1993, MNRAS, 261, 175
Zheng, Z. Y., Shang, Z. H., & Su, H. J. 1999, AJ, 117, 2757
Zhou, X., Chen, J., Xu, W., Zhang, M., Jiang, Z., Zhang, Z., & Zhu, J. 1999, PASP, 111, 909
Zhou, X., Jiang, Z.-J., Xue, S.-J., Wu, H., Ma, J., & Chen, J.-S. 2001, Chinese J. Astron. Astrophys., 1, 372
Zhou, X., et al. 2003, A&A, 397, 361
———. 2004, AJ, 127, 3642